

# A Cone Beam Computed Tomography Annotation Tool for Automatic Detection of the Inferior Alveolar Nerve Canal

Cristian Mercadante<sup>1</sup>, Marco Cipriano<sup>1</sup>, Federico Bolelli<sup>1</sup>, Federico Pollastri<sup>1</sup>,  
Mattia Di Bartolomeo<sup>2</sup>, Alexandre Anesi<sup>3</sup> and Costantino Grana<sup>1</sup>

<sup>1</sup>Department of Engineering “Enzo Ferrari”,

University of Modena and Reggio Emilia, Via P. Vivarelli 10, 41125 Modena, Italy

<sup>2</sup>Surgery, Dentistry, Maternity and Infant Department, Unit of Dentistry and Maxillo-Facial Surgery,  
University of Verona, P.le L.A. Scuro 10, 37134 Verona, Italy

<sup>3</sup>Department of Medical and Surgical Sciences for Children & Adults, Cranio-Maxillo-Facial Surgery,  
University of Modena and Reggio Emilia, Largo del Pozzo 71, 41124 Modena, Italy

Keywords: CBCT, IAC, IAN, Annotation Tool, Segmentation.

Abstract: In recent years, deep learning has been employed in several medical fields, achieving impressive results. Unfortunately, these algorithms require a huge amount of annotated data to ensure the correct learning process. When dealing with medical imaging, collecting and annotating data can be cumbersome and expensive. This is mainly related to the nature of data, often three-dimensional, and to the need for well-trained expert technicians. In maxillofacial imagery, recent works have been focused on the detection of the Inferior Alveolar Nerve (IAN), since its position is of great relevance for avoiding severe injuries during surgery operations such as third molar extraction or implant installation. In this work, we introduce a novel tool for analyzing and labeling the alveolar nerve from Cone Beam Computed Tomography (CBCT) 3D volumes.

## 1 INTRODUCTION

Maxillofacial surgery is a medical-surgical field that concerns the diagnosis and treatment of a wide variety of head and neck pathologies, including functional and aesthetic problems. Maxillofacial surgical interventions comprise oral and dental operations. Among the cited surgical interventions, the extraction of impacted teeth (especially third molars) and the implant-prosthetic rehabilitation are two of the most common procedures. This kind of surgical interventions are routinely executed and may become very tricky due to the risk of damaging the Inferior Alveolar Nerve (IAN).

This sensory nerve supplies the omolateral sensibility to part of the lower third of the face and of the inferior dental arch. In order to preserve this noble structure during the surgery, an accurate preoperative planning must be done and has to include the localization of the IAN. Its position might be indirectly deduced via the individuation of the mandibular canal, also known as Inferior Alveolar Canal (IAC), which runs inside the mandibular bone. The nerve might be in close relation to the roots of impacted teeth (es-

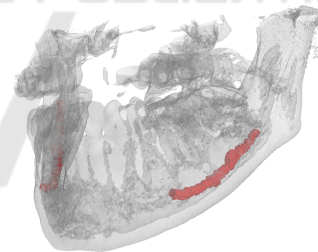


Figure 1: 3D view of a jawbone (gray) underlying the location of the IAC (red). The original volume has been acquired with Cone Beam Computed Tomography.

pecially the molars) and a detailed 3D description of their positions must be comprehended before the surgery. A dental implant consists in the surgical insertion of an artificial root into the jawbone to provide anchorage for a dental prosthesis replacing the missing tooth (implant-prosthetic rehabilitation). To this purpose, to plan and place accurately a dental implant it is mandatory to know the linear distance from the midpoint of the alveolar crest to the IAC.

In order to facilitate the identification of the IAN, many computer-based techniques have been proposed in the past. Most of the approaches available in the

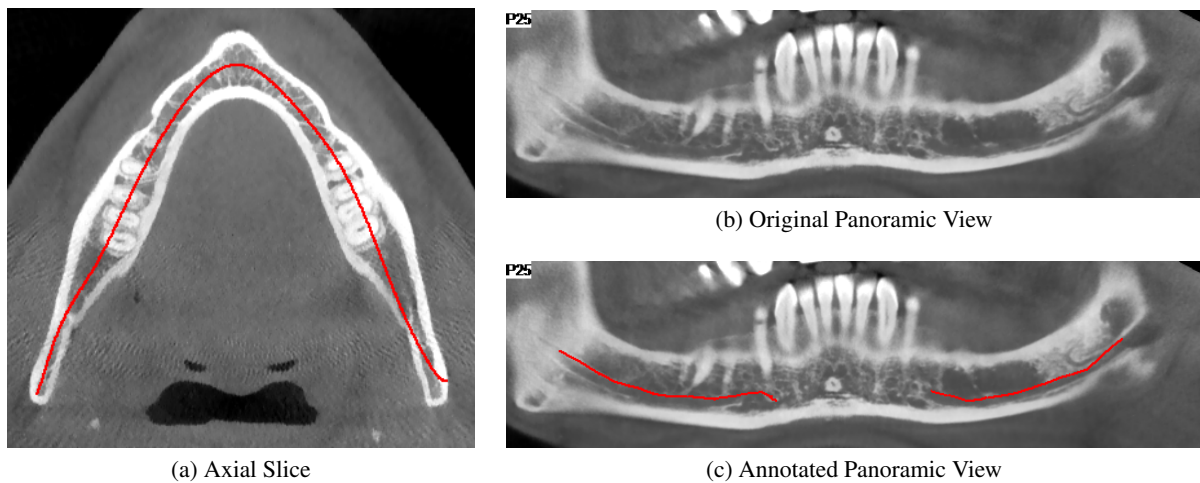


Figure 2: Example of CT annotation based on 2D panoramic views. (a) is an axial slice of the CT where a panoramic base curve is highlighted in red. (b) is the panoramic view obtained from the CT-volume displaying voxels of the curved plane generated by the base curve and orthogonal to the axial view. (c) is the same view of (b) showing a manual annotation of the IAC performed by an expert technician. A 3D view of the CT scan with the same annotation as (c) is reported in Figure 3.

literature focus on the identification of the IAC. As a matter of fact, the canal is clearly identifiable in both 2D panoramic radiography —also named OrthoPantomogram (OPG)— and Computed Tomography (CT) (Sotthivirat and Narkbuakaew, 2006).

Algorithms based on panoramic radiography reported higher accuracy (Vinayahalingam et al., 2019). However, OPG images just show the IAN from a single point of view, masking the real complexity of the 3D canal structure. Moreover, such a kind of images usually provide geometrical distorted data (Abrahams, 2001) and no information about depth (Sotthivirat and Narkbuakaew, 2006). This is why state-of-the-art approaches tackle the task considering the entire 3D volume obtained with CT scanners (Kondo et al., 2004; Kwak et al., 2020). These three-dimensional data can be reformatted into panoramic reconstructions (panoramic views) thus being able to apply 2D strategies also on 3D data. With respect to OPG, panoramic reconstructions are not affected by distortion, superimposition of other tissues or magnification errors, permitting a more accurate assessment of CT data.

In recent years, deep learning algorithms have revealed to be extremely effective solutions to tackle multiple image processing and computer vision tasks. In particular, Convolutional Neural Networks (CNNs) are currently the cornerstone of medical image analysis (Ronneberger et al., 2015; Esteva et al., 2017; Canalini et al., 2019; Pollastri et al., 2019; Ligabue et al., 2020; Pollastri et al., 2021). These techniques have been recently applied also to the segmentation of the IAC (Vinayahalingam et al., 2019; Hwang et al., 2019; Kwak et al., 2020). Unfortunately, they require

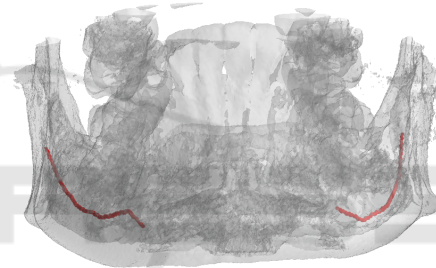


Figure 3: 3D view of the manual annotation performed by an expert technician on the panoramic of Figure 2c.

huge amounts of data, which are hard to obtain and particularly expensive to annotate, especially in medical fields. However, simple elements like lines and colors are learned from the first convolutional layers of CNNs models. For this reason, neural networks pre-trained with existing collections of natural images can mitigate the need for large annotated medical datasets (Deng et al., 2009; Li et al., 2015).

Nevertheless, this approach can not be the panacea since it may introduce biases towards certain characteristics and features. As an example, CNNs trained using ImageNet are strongly biased in recognizing textures rather than shapes (Geirhos et al., 2018).

Several proprietary tools for annotating the inferior alveolar canal from computed tomography scans are available in the literature. Such tools are usually supplied together with CT scanners and not otherwise accessible. Moreover, most of them only provide two dimensional annotation mechanisms based on panoramic reconstructions from CT data (an explanatory example is reported in Figure 2).

This paper proposes a novel IAC Annotation Tool (IACAT in short) that aims to overcome the aforementioned limitations, guaranteeing a more accurate annotation while speeding up and simplifying the manual effort of expert technicians.

In Section 2, imaging techniques for maxillofacial surgery and deep learning approaches for the automatic detection of the inferior alveolar nerve are detailed, focusing on the employed data. Section 3 describes the annotation tool released with this paper. Finally, some conclusions are drawn in Section 4.

## 2 RELATED WORK

### 2.1 Imaging for Maxillofacial Surgery

Many imaging techniques have been used in the past for implant dentistry. Among them, OrthoPantomogram (OPG), Computed Tomography (CT), and Cone Beam Computed Tomography (CBCT) are certainly the most widespread. In clinical research, CBCT is increasingly being used for 3D assessment of bone and soft tissue (Benic et al., 2015).

The term orthopantomogram, orthopantomography, panoramic tomography or OPG in short, refers to panoramic single image radiography of the mandible, maxilla and teeth. This technique is based on X-ray and the OPG unit is designed to rotate around the head of the patient during the scan. It represents an inexpensive and rapid way to evaluate the gross anatomy of the jaws and related structures, but its limits are bidimensionality and structure distortion.

Computed Tomography, instead, refers to a computerized X-ray imaging procedure that provides more complete and detailed information than OPG.

CT employs a narrow beam of X-rays and the machine emitting this beam quickly rotated around the body, producing signals that are then processed by a computer. The output of the CT scanner are cross-sectional images (slices) of the analyzed body section. Sequential slices can be digitally stacked to form a 3D volume, allowing for easier identification and location of basic structures.

Cone Beam Computed Tomography is a variation of the traditional Computed Tomography and represents the most commonly employed 3D imaging modality in dentistry, both for treatment planning and postoperative evaluation (Jaju and Jaju, 2014).

A CBCT scanner employs a cone beam radiating from an X-ray source in the shape of a cone. The use of this particular shape allows to cover large volumes while performing a single rotation around the

patient. CBCT imaging is powerful and presents a decreased effective radiation dose exposure to patients compared to traditional multi-slice CT (Silva et al., 2008; Ludlow and Ivanovic, 2008; Loubele et al., 2009; Carrafiello et al., 2010)

The entire 3D volume is then reconstructed processing acquired data with specific algorithms. A sample view of CBCT-acquired 3D volume is reported in Figure 1.

### 2.2 IAC Automatic Detection

Given the relevance of the task, many efforts have been given to employ computer vision for IAC automatic detection. The first approach (Kondo et al., 2004) consisted in reformatting the original CT images to obtain panoramic reconstructions from CT data (panoramic views), which are a series of cross-sectional images along the mandible (lower jawbone). Voxel intensities and 3D gradients are then exploited to identify empty canals in the panoramic views. The axis of the IAC is then traced out by a 3D line-tracking technique, effectively extracting the IAC despite the open structure of the surrounding bone.

In the same year, Hanssen et al. presented a method for 3D segmentation of the same nerve channels in the human mandible. Their technique utilizes geodesic active surfaces, implemented with level sets, and consists of two steps. For the first step, two points are defined to denote the entry and exit of the nerve channel, and a connecting path of minimal action inside the channel is calculated. This calculation is driven by the gray values in proximity to the two defined points inside the channel. For the next step, the authors exploit this path as an initial configuration, and let an active surface evolve until the inner borders of the channel are reached (Hanssen et al., 2004).

Two years later a new technique was introduced to automatically detect the alveolar nerve canals on panoramic reconstructions from CT data (Sotthivirat and Narkbuakaew, 2006). By using a set of axial CT images acquired from the CT scanner, a series of panoramic images are generated along the dental curve. Generated images are then processed by means of contrast enhancement and Gaussian smoothing filtering before being fed to a detection algorithms based on the distance transform of the edge image, morphological operations, and an approximation of the nerve canals shape.

In more recent times this task has been affected, as the the rest of the medical imaging area, by the groundbreaking rise of deep learning. In 2019, Vinayahalingam et al. focus on detecting the IAN and the third molar in Orthopantomogram Panoramic Ra-

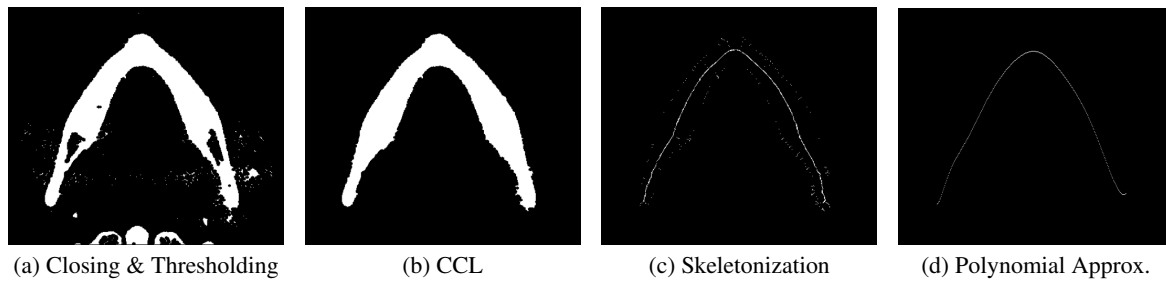


Figure 4: Automatic arch detection steps.

diographs (OPG) (Vinayahalingam et al., 2019).

The authors claim that specific radiographic features on OPGs such as darkening of the root, narrowing of the mandibular canal, interruption of the white line, are risk factors for IAN injuries. Accordingly, they employ deep learning in the detection of third molars, mandibular canals, and for the identification of certain radiological signs for potential IAN injuries.

The following year, a preliminary research for a dental segmentation automation tool on CT scans has been published (Kwak et al., 2020). In this paper, a set of experiments were conducted on models based on 2D SegNet (Badrinarayanan et al., 2017), 2D and 3D U-Net (Ronneberger et al., 2015; Çiçek et al., 2016).

### 3 THE IAC ANNOTATION TOOL

Most of the datasets employed in literature for the automatic segmentation of the inferior alveolar nerve have been annotated using proprietary software, e.g. Photoshop<sup>1</sup> and Invivo<sup>2</sup>. However, working with 3D data can be laborious and time-consuming. This paper proposes a tool for smoothing the burden of manual annotation, specifically designed for the IAN canal. It processes and visualizes CBCT data stored in DICOM format, driving the user towards the annotation of axial images, panoramic and cross-sectional views. Annotated data can be easily exported to be employed in multiple tasks, e.g. the training of deep learning models.

#### 3.1 Pre-processing

The tool requires a DICOM input, in particular a DICOMDIR file linked to dcm files, representing single axial images of the scan. Radiography values represent attenuation of the X-rays emitted and captured by a detector. These measures are always considered

<sup>1</sup><https://www.photoshop.com>

<sup>2</sup><https://www.anatomage.com/invivo>

on the Hounsfield scale, where higher numbers indicate a high attenuation. After loading the scan volume, a saturation threshold is applied: bone voxels have Hounsfield units usually in the range [400, 3000] (Nysjö, 2016), but peak values around 14000 usually correspond to the tooth crown and enamel (less of 2% of the volume). Since the IAN canal is not involved in this operation, it is reasonable to saturate from the top with the 0.98 percentile value. The values are then normalized in the range [0, 1] and stored as 32 bits floating point values without losing any information. This pre-processing acts as a contrast stretching of the original DICOM values.

#### 3.2 Axial Image Annotation

After loading the input data, the arch approximation that better describes the canal course must be identified inside one of the axial images. This process is partially automated and aims to segment the gums region in order to obtain a skeleton and to approximate it with a polynomial. A morphological closing (Gil and Kimmel, 2002) with an elliptical  $5 \times 5$  structuring element is applied in order to close gaps inside foreground regions. Then, the image is binarized by selecting the threshold value so that foreground pixels are between 12% to 16% of the image. Connected Components Labeling (CCL) (Bolelli et al., 2019) is employed to keep only the biggest object — the gums — by removing all the other components. Inner holes are filled with a second CCL pass, producing a binary image with the gums region appearing as a filled arch. Image skeletonization is then performed using thinning (Bolelli and Grana, 2019). The output is a one pixel thick curve crossing the dental arch, which is approximated with a polynomial. The entire process is depicted in Figure 4.

Once the axial image and its arch approximation are selected, the tool generates a Catmull-Rom spline (Catmull and Rom, 1974; Barry and Goldman, 1988) by sampling the polynomial to select the control points of the spline. This curve is the base of a Curved Planar Reformation (CPR) that produces

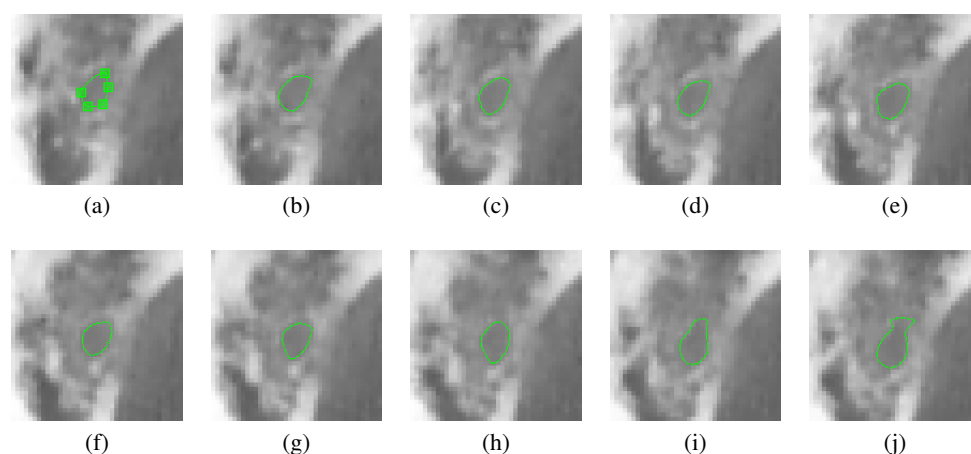


Figure 5: Morphological Geodesic Active Contours evolution on a sequence of cross-sectional images.

a panoramic 2D image. This view is obtained displaying voxels of the curved plane corresponding the base curve and orthogonal to the axial slice. When the user moves, creates or removes control points, the panoramic view changes accordingly. The goal of this step is to highlight the IAC on the panoramic view, by finding the best arch curve. The user can also offset the position of this curve in order to produce an upper and lower panoramic view, thus ensuring a better editing of the spline itself (Sotthivirat and Narkbuakaew, 2006).

Two offset curves (outer and inner) are drawn with distance 50 pixels from the main arch. For each point of the spline, a perpendicular line called *Cross-Sectional Line* (CSL) is computed. Since the points of the spline are as many as the euclidean distance between two control points, a different resolution of the spline would generate more or less CSLs. These lines are the base of Multi Planar Reformations (MPRs) called *Cross-Sectional Views* (CSVs). These are 2D images obtained interpolating the values of the respective base line across the whole volume height.

### 3.3 Annotating Cross-sectional Views

For each CSV, the user can draw a closed Catmull-Rom spline to annotate the position of the IAC. As usual, control points can be created, deleted, or moved. To speed-up the annotation phase, an active contour model (Kass et al., 1988) is used to automatically propagate the annotation to the following image. In particular, Morphological Geodesic Active Contours have been selected (Caselles et al., 1997; Alvarez et al., 2010): this technique employs morphological operators to evolve the curve, combined with the concept of energy minimization in the problem of geodesic curve computation. In absence of

gradients, this algorithm forces the contour to expand—the balloon factor— whereas other active contour approaches shrink object shapes.

In order to propagate the annotation to the following (or previous) cross-sectional view, the Morphological Geodesic Active Contours algorithm requires two inputs: the current annotation as a binary mask, and the gradients of the following (or previous) CSV. The output of the algorithm is a new annotation mask from which the tool generates the spline with an amount of control points that depends on its length (the longer it is, the more control points are needed to approximate the real shape). The model runs for 5 iterations, with a smoothing factor of 1, and a balloon factor of 1. Figure 5 shows the evolution of the spline in subsequent images, starting from a manual annotation, up to the ninth following image. The model is able to create accurate annotations without user intervention for many consecutive images. In this example, the first mistake appears in Figure 5i (the top edge of the spline), and is propagated into Figure 5j.

Any user adjustment can be automatically propagated to the following views.

The splines are saved as the coordinates of their control points, and a label mask is generated for each CSV. The labels employed are four (Çiçek et al., 2016): *unlabeled*, *background*, *contour*, *interior*. Images that are not annotated inherit *unlabeled* class by default. Otherwise, the mask is set to *background*, with the spline labeled as *contour* and internal pixels labeled as *interior*.

### 3.4 Tilted Cross-sectional Views

An important feature introduced in the IACAT tool is the extraction of CSVs orthogonal to the canal slope. To achieve this goal, the Cross-Sectional

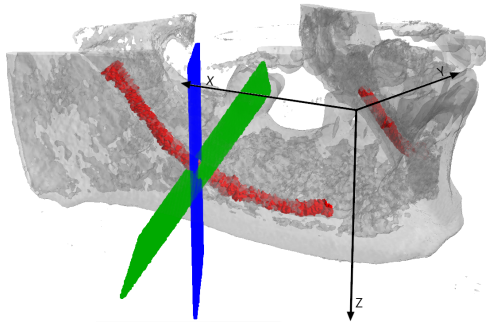


Figure 6: A visualization of the cross-sectional plane rotation around the  $y$  axis, as described in Section 3.4. The original plane is presented in blue, whereas the tilted one is green. The IAC is red.

Planes (CSPs) used for generating the CSVs are tilted accordingly.

On the panoramic view, the user can draw two Catmull-Rom splines which indicate the canal position, one for each branch. For each point  $p$  of the spline, the slope can be computed by using the derivative of a  $12^{th}$  order polynomial fit  $f$ :

$$\beta(p) = -\arctan(f'(p)) \quad (1)$$

Given the slope of the canal, the cross-sectional view orthogonal to the canal is obtained as follows:

- The cross-sectional plane is translated so that its center is placed at the origin of the reference system;
- The plane is rotated around the  $z$  axis, until it becomes parallel to the  $y$  axis. The following Equation shows the rotation matrix, where  $u$  is the unit vector of the plane:

$$\begin{bmatrix} u_y & -u_x & 0 \\ u_x & u_y & 0 \\ 0 & 0 & 1 \end{bmatrix} \quad (2)$$

- The plane is then rotated around the  $y$  axis, by the angle  $\beta$  obtained with Equation 1, using the following rotation matrix:

$$\begin{bmatrix} \cos \beta & 0 & \sin \beta \\ 0 & 1 & 0 \\ \sin \beta & 0 & \cos \beta \end{bmatrix} \quad (3)$$

- Finally, the plane is rotated back around the  $z$  axis to its original position, using the rotation matrix in Equation 4, and the initial translation is reversed.

$$\begin{bmatrix} u_y & u_x & 0 \\ -u_x & u_y & 0 \\ 0 & 0 & 1 \end{bmatrix} \quad (4)$$

The CSVs are generated from the rotated planes, using bilinear interpolation. In most cases, since the

canal has a slight inclination, the tilted cross-sectional views do not differ much from the straight ones. Figure 7 shows two examples in which tilted views provide strong improvements to the IAC localization.

### 3.5 Annotation Re-projection

The re-projection of the labeled masks in 3D is required to generate the final segmentation. A plane corresponds to each cross-sectional image, which contains the floating point coordinates of the volume voxels used to interpolate a certain pixel in the image. For each pixel of the image, its label is re-projected in the corresponding voxel coordinate. To prevent aliasing due to the undersampling of the voxel coordinates in the volume, each label is copied to the positions corresponding to the *floor* and *ceil* of each coordinate of the plane. Figure 8 shows the results obtained re-projecting straight cross-sectional images annotation masks in 3D (considering only *contour* and *interior* labels).

The surface of the reconstructed volume is often irregular, due to the nature of the 2D annotations.

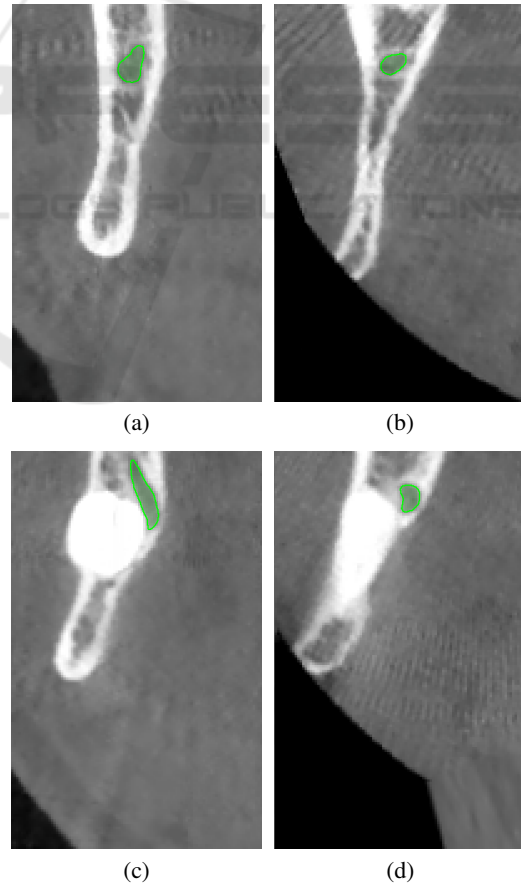


Figure 7: Comparison of straight (a), (c) and tilted (b), (d) cross-sectional images.

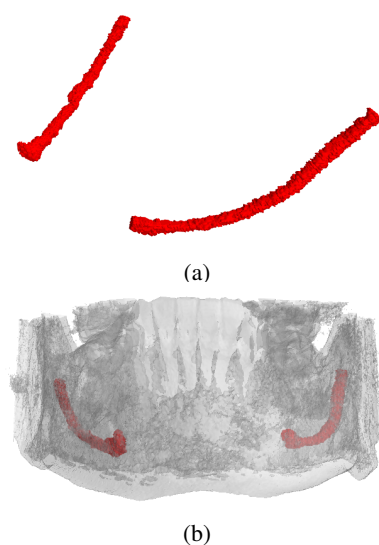


Figure 8: (a) 3D view of the canal reconstruction and (b) its location inside the jawbone.

Therefore, a smoothing process is proposed to produce a polished contour on the 3D canal shape. A  $22 \times 22 \times 22$  kernel is moved with stride 18 along the reconstructed canal volume. At each step, the convex hull is evaluated on the current block, obtaining a set of triangles that composes the convex hull. These triangles are then voxelized and the smoothed canal is created. The described approach generate a more regular and uniform segmentation at the expense of the final accuracy.

### 3.6 Exports

The annotation can finally be exported as binary `numpy` files. The two main formats are the concatenation of cross-sectional image masks and the re-projected 3D annotation. The tool is also able to generate `png` images, both for cross-sectional images and their labeled masks, and to create a new `DICOM` file with annotations as overlays. An important feature of the tool is the recording of user actions, in particular of every interaction with the splines (on axial images, panoramic views and cross-sectional images). Indeed, future research directions include the automation of more steps in the annotation process, by learning from the actions of an expert. Therefore, creation, removal and changes in splines control points are recorded, with contextual information, such as the current cross-sectional image index. Moreover, the tool records whether the user is propagating the annotations or resetting the current spline. The history of actions can be saved on disk in `json` format.

## 4 CONCLUSION

In this paper we presented IACAT, a software for the annotation of CBCT scans. The proposed tool comprises and improves the functionality of existing annotation tools for the segmentation of Inferior Alveolar Nerve, simplifying and improving the work of expert technicians. The image processing techniques implemented allow to automatically extend manual annotations carried out on portions of the volume, thus speeding up the entire process.

## REFERENCES

- Abrahams, J. J. (2001). Dental ct imaging: A look at the jaw. *Radiology*, 219(2):334–345.
- Alvarez, L., Baumela, L., Henriquez, P., and Marquenez-Neila, P. (2010). Morphological snakes. In *2010 IEEE Computer Society Conference on Computer Vision and Pattern Recognition*, pages 2197–2202.
- Badrinarayanan, V., Kendall, A., and Cipolla, R. (2017). SegNet: A Deep Convolutional Encoder-Decoder Architecture for Image Segmentation. *IEEE Transactions on Pattern Analysis and Machine Intelligence*, 39:2481–2495.
- Barry, P. and Goldman, R. (1988). A Recursive Evaluation Algorithm for a Class of Catmull-Rom Splines. *ACM SIGGRAPH Computer Graphics*, 22:199–204.
- Benic, G. I., Elmasry, M., and Hämmerle, C. H. (2015). Novel digital imaging techniques to assess the outcome in oral rehabilitation with dental implants: a narrative review. *Clinical Oral Implants Research*, 26:86–96.
- Bolelli, F., Allegretti, S., Baraldi, L., and Grana, C. (2019). Spaghetti Labeling: Directed Acyclic Graphs for Block-Based Connected Components Labeling. *IEEE Transactions on Image Processing*, 29(1):1999–2012.
- Bolelli, F. and Grana, C. (2019). Improving the Performance of Thinning Algorithms with Directed Rooted Acyclic Graphs. In *Image Analysis and Processing - ICIAP 2019*, volume 11752, pages 148–158. Springer.
- Canalini, L., Pollastri, F., Bolelli, F., Cancilla, M., Allegretti, S., and Grana, C. (2019). Skin Lesion Segmentation Ensemble with Diverse Training Strategies. In *Computer Analysis of Images and Patterns*, volume 11678, pages 89–101. Springer.
- Carrafello, G., Dizonno, M., Colli, V., Strocchi, S., Taubert, S. P., Leonardi, A., Giorgianni, A., Barresi, M., Macchi, A., Bracchi, E., et al. (2010). Comparative study of jaws with multislice computed tomography and cone-beam computed tomography. *La radiologia medica*, 115(4):600–611.
- Caselles, V., Kimmel, R., and Sapiro, G. (1997). Geodesic Active Contours. *International Journal of Computer Vision*, 22:61–79.
- Catmull, E. and Rom, R. (1974). A Class of Local Interpolating Splines. *Computer Aided Geometric Design - CAGD*, 74:317–326.

- Çiçek, O., Abdulkadir, A., Lienkamp, S., Brox, T., and Ronneberger, O. (2016). 3D U-Net: Learning Dense Volumetric Segmentation from Sparse Annotation. In *International Conference on Medical Image Computing and Computer-Assisted Intervention*, pages 424–432.
- Deng, J., Dong, W., Socher, R., Li, L.-J., Li, K., and Fei-Fei, L. (2009). ImageNet: A Large-Scale Hierarchical Image Database. In *2009 IEEE Conference on Computer Vision and Pattern Recognition*, pages 248–255. IEEE.
- Esteva, A., Kuprel, B., Novoa, R. A., Ko, J., Swetter, S. M., Blau, H. M., and Thrun, S. (2017). Dermatologist-level classification of skin cancer with deep neural networks. *Nature*, 542(7639):115–118.
- Geirhos, R., Rubisch, P., Michaelis, C., Bethge, M., Wichmann, F. A., and Brendel, W. (2018). ImageNet-trained CNNs are biased towards texture; increasing shape bias improves accuracy and robustness. *arXiv preprint arXiv:1811.12231*.
- Gil, J. Y. and Kimmel, R. (2002). Efficient Dilation, Erosion, Opening, and Closing Algorithms. *IEEE Transactions on Pattern Analysis and Machine Intelligence*, 24(12):1606–1617.
- Hanssen, N., Burgielski, Z., Jansen, T., Lievin, M., Ritter, L., von Rymon-Lipinski, B., and Keeve, E. (2004). Nerves-level sets for interactive 3d segmentation of nerve channels. In *2004 2nd IEEE International Symposium on Biomedical Imaging: Nano to Macro (IEEE Cat No. 04EX821)*, volume 1, pages 201–204.
- Hwang, J.-J., Jung, Y.-H., Cho, B.-H., and Heo, M.-S. (2019). An overview of deep learning in the field of dentistry. *Imaging science in dentistry*, 49(1):1–7.
- Jaju, P. P. and Jaju, S. P. (2014). Clinical utility of dental cone-beam computed tomography: current perspectives. *Clinical, cosmetic and investigational dentistry*, 6:29.
- Kass, M., Witkin, A., and Terzopoulos, D. (1988). Snakes: Active contour models. *International Journal of Computer Vision*, 1(4):321–331.
- Kondo, T., Ong, S., and Foong, K. W. (2004). Computer-based extraction of the inferior alveolar nerve canal in 3-D space. *Computer Methods and Programs in Biomedicine*, 76(3):181–191.
- Kwak, H., Kwak, E.-J., Song, J.-M., Park, H., Jung, Y.-H., Cho, B.-H., Hui, P., and Hwang, J. (2020). Automatic mandibular canal detection using a deep convolutional neural network. *Scientific Reports*, 10.
- Li, Y., Yosinski, J., Clune, J., Lipson, H., and Hopcroft, J. E. (2015). Convergent Learning: Do different neural networks learn the same representations? In *Proceedings of the 1st International Workshop on Feature Extraction: Modern Questions and Challenges at NIPS 2015*, pages 196–212.
- Ligabue, G., Pollastri, F., Fontana, F., Leonelli, M., Furci, L., Giovanella, S., Alfano, G., Cappelli, G., Testa, F., Bolelli, F., Grana, C., and Magistroni, R. (2020). Evaluation of the Classification Accuracy of the Kidney Biopsy Direct Immunofluorescence through Convolutional Neural Networks. *Clinical Journal of the American Society of Nephrology*, 15(10):1445–1454.
- Loubele, M., Bogaerts, R., Van Dijck, E., Pauwels, R., Vanheusden, S., Suetens, P., Marchal, G., Sanderink, G., and Jacobs, R. (2009). Comparison between effective radiation dose of CBCT and MSCT scanners for dentomaxillofacial applications. *European Journal of Radiology*, 71(3):461–468.
- Ludlow, J. B. and Ivanovic, M. (2008). Comparative dosimetry of dental CBCT devices and 64-slice CT for oral and maxillofacial radiology. *Oral Surgery, Oral Medicine, Oral Pathology, Oral Radiology, and Endodontology*, 106(1):106–114.
- Nysjö, J. (2016). *Interactive 3D Image Analysis for Cranio-Maxillofacial Surgery Planning and Orthopedic Applications*. PhD thesis, Uppsala University.
- Pollastri, F., Bolelli, F., Paredes, R., and Grana, C. (2019). Augmenting Data with GANs to Segment Melanoma Skin Lesions. *Multimedia Tools and Applications Journal*, 79(21-22):15575–15592.
- Pollastri, F., Maroñas, J., Bolelli, F., Ligabue, G., Paredes, R., Magistroni, R., and Grana, C. (2021). Confidence Calibration for Deep Renal Biopsy Immunofluorescence Image Classification. In *2020 25th International Conference on Pattern Recognition (ICPR)*.
- Ronneberger, O., Fischer, P., and Brox, T. (2015). U-Net: Convolutional Networks for Biomedical Image Segmentation. *LNCS*, 9351:234–241.
- Silva, M. A. G., Wolf, U., Heinicke, F., Bumann, A., Visser, H., and Hirsch, E. (2008). Cone-beam computed tomography for routine orthodontic treatment planning: a radiation dose evaluation. *American Journal of Orthodontics and Dentofacial Orthopedics*, 133(5):640–e1.
- Sotthivirat, S. and Narkbuakaew, W. (2006). Automatic Detection of Inferior Alveolar Nerve Canals on CT Images. In *2006 IEEE Biomedical Circuits and Systems Conference*, pages 142–145.
- Vinayahalingam, S., Xi, T., Berge, S., Maal, T., and De Jong, G. (2019). Automated detection of third molars and mandibular nerve by deep learning. *Scientific Reports*, 9.